The OWLeS IOP2b Lake-Effect Snowstorm: Mechanisms Contributing to the Tug Hill Precipitation Maximum

LEAH S. CAMPBELL AND W. JAMES STEENBURGH

Department of Atmospheric Sciences, University of Utah, Salt Lake City, Utah

(Manuscript received 12 December 2016, in final form 23 February 2017)

ABSTRACT

Lake-effect storms frequently produce a pronounced precipitation maximum over the Tug Hill Plateau (hereafter Tug Hill), which rises 500 m above Lake Ontario's eastern shore. Here Weather Research and Forecasting Model simulations are used to examine the mechanisms responsible for the Tug Hill precipitation maximum observed during IOP2b of the Ontario Winter Lake-effect Systems (OWLeS) field program. A key contributor was a land-breeze front that formed along Lake Ontario's southeastern shoreline and extended inland and northeastward across Tug Hill, cutting obliquely across the lake-effect system. Localized ascent along this boundary contributed to an inland precipitation maximum even in simulations in which Tug Hill was removed. The presence of Tug Hill intensified and broadened the ascent region, increasing parameterized depositional and accretional hydrometeor growth, and reducing sublimational losses. The inland extension of the land-breeze front and its contribution to precipitation enhancement appear to be unidentified previously and may be important in other lake-effect storms over Tug Hill.

1. Introduction

Lake-effect snowstorms generated over the Great Lakes of North America and other bodies of water can produce intense, extremely localized snowfall (e.g., Andersson and Nilsson 1990; Steenburgh et al. 2000; Eito et al. 2005; Laird et al. 2009; Kindap 2010). Forecasters still struggle, however, to accurately predict the timing and location of the heaviest snowfall during lake-effect events, which disrupt local and regional transportation, education, utilities, and commerce (e.g., Carpenter 1993; Norton and Bolsenga 1993; Schmidlin 1993). The presence of terrain further complicates lake-effect prediction, such as over the modest Tug Hill Plateau (hereafter Tug Hill), which, at a gradual slope of ~1.25% and over 20–30 km, rises ~500 m above the eastern shore of Lake Ontario and receives more than twice the annual lake-effect precipitation than the surrounding lowlands (Veals and Steenburgh 2015).

Climatological precipitation maxima are found over terrain features downstream of lake- and sea-effect-producing bodies of water such as the Great Lakes, the Great Salt Lake, and the Sea of Japan (e.g., Norton and Bolsenga 1993; Murakami et al. 1994; Nakai and Endoh 1995; Yeager et al. 2013; Veals and Steenburgh 2015). Even small topographic features such as the hills, plateaus, and upland regions downstream of the Great Lakes can dramatically enhance lake-effect precipitation (e.g., Hill 1971; Hjelmfelt 1992). Moist flow over such orography can produce or enhance precipitation, which depends on a combination of factors such as the large-scale storm environment, incident flow characteristics, terrain geometry, ambient stability and humidity, and microphysical time scales and processes (e.g., Houze 2012). Although orographic effects on precipitation have been studied extensively in a variety of contexts [see reviews by Roe (2005), Smith (2006), Houze (2012), Colle et al. (2013), and Stoelinga et al. (2013)], the physical mechanisms producing orographic precipitation enhancement during lake-effect storms have yet to be fully elucidated.

Minder et al. (2015) summarize some potential mechanisms for the precipitation maxima found over topographic features during lake-effect storms. These mechanisms include the following: 1) lifting of the inversion layer and subsequent invigoration of convection through increased updraft speed and/or cloud depth (e.g., Murakami et al. 1994), 2) broadening of the scale of existing convective cells (e.g., Kirshbaum and Grant 2012; Minder et al. 2013), 3) triggering of new convection and increase in convective frequency (e.g.,

Corresponding author e-mail: Leah S. Campbell, leah.campbell@utah.edu

DOI: 10.1175/MWR-D-16-0461.1

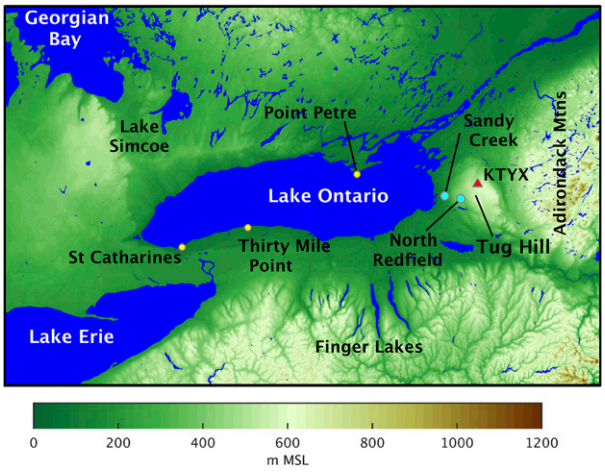

FIG. 1. Topographic and geographic features of the eastern Great Lakes and Lake Ontario, from USGS 30-arc-s topography. Elevation (m MSL) shaded following scale at bottom.

Browning et al. 1974; Colle et al. 2008; Smith et al. 2009), 4) the seeder–feeder effect (e.g., Bergeron 1965), 5) a convective-to-stratiform transition (e.g., Yuter and Houze 1995) that more efficiently produces surface snowfall, 6) orographic suppression of subcloud sublimation (Murakami et al. 1994), and 7) favorable lofting and transport of hydrometeors from upstream, overlake ascent regions (Alcott and Steenburgh 2013). Patterns of ascent and hydrometeor advection within lake-effect storms and over downstream terrain are further complicated by the mesoscale circulation of the lake-effect system itself (e.g., Bergmaier et al. 2017) and by land-breeze circulations forced by factors such as thermal contrasts, differential surface roughness, ice cover, and shoreline geometry around the lake (e.g., Steenburgh and Campbell 2017).

The December 2013–January 2014 Ontario Winter Lake-effect Systems (OWLeS) field program was a multi-institutional effort sponsored by the National Science Foundation to examine lake-effect systems over and downstream of Lake Ontario, including the enhancement of long-lake-axis-parallel (LLAP) lake-effect systems over Tug Hill (Kristovich et al. 2017). Vertically profiling and airborne cloud radar observations from OWLeS IOP2b (2300 UTC 10 December–0200 UTC 12 December 2013), which produced 101.5 cm of snow on Tug Hill in 24 h (Campbell et al. 2016), reveal a transition from deeper, stronger, and more turbulent echoes near the Lake Ontario shoreline to shallower, more persistent, and less turbulent echoes inland and over Tug Hill (Minder et al. 2015; Welsh et al. 2016). Such results are consistent with a convective-to-stratiform transition rather than an invigoration of convection, and statistics from 29 additional lake-effect events sampled by profiling radars show that such a transition is common over Tug Hill (Minder et al. 2015). Campbell et al. (2016) examined variations in enhancement over Tug Hill during IOP2b and found that intense LLAP bands produced the highest precipitation rates, but the smallest ratio of upland to lowland precipitation. In contrast, nonbanded periods produced smaller precipitation rates, but a larger ratio of upland to lowland precipitation, leading to the event-total precipitation maximum over Tug Hill. These observational studies were constrained, however, by the inherent limitations of the observational datasets and were unable to fully investigate the potential enhancement mechanisms.

This paper uses Weather Research and Forecasting (WRF) Model simulations to build on the findings of Minder et al. (2015), Campbell et al. (2016), and Welsh et al. (2016) to further our understanding of the mechanisms producing the Tug Hill precipitation maximum during OWLeS IOP2b. We describe the observational datasets and model configuration in section 2 and provide an event overview and model validation in section 3. Contributors to the Tug Hill precipitation maximum are examined in sections 4, 5, and 6. Conclusions follow in section 7.

2. Data and methods

a. *Observational datasets*

To validate the numerical simulations presented here we use observations collected during the OWLeS field program. Surface observations of wind, temperature, relative humidity, and automated and manual observations of liquid precipitation equivalent (hereafter referred to simply as precipitation) were collected at Sandy Creek (SC), a lowland (175 m MSL) site at the base of Tug Hill, and North Redfield (NR), an upland (385 m MSL) site near the climatological precipitation maximum on Tug Hill (see Fig. 1 for locations). Campbell et al. (2016) describe these sites and observations in detail. Vertical profiles of wind, temperature, and dewpoint were obtained using GRAW GPS-based upper-air soundings launched from NR at 1- to 3-h intervals.

Radar reflectivity data from the Weather Surveillance Radar-1988 Doppler (WSR-88D) located on Tug Hill at Montague, New York (KTYX; Fig. 1), were downloaded from the National Climatic Data Center (NCDC) Next Generation Weather Radar (NEXRAD) archive in level II format (Crum et al. 1993). Additionally, following Campbell et al. (2016), we estimate the precipitation distribution over Tug Hill using an

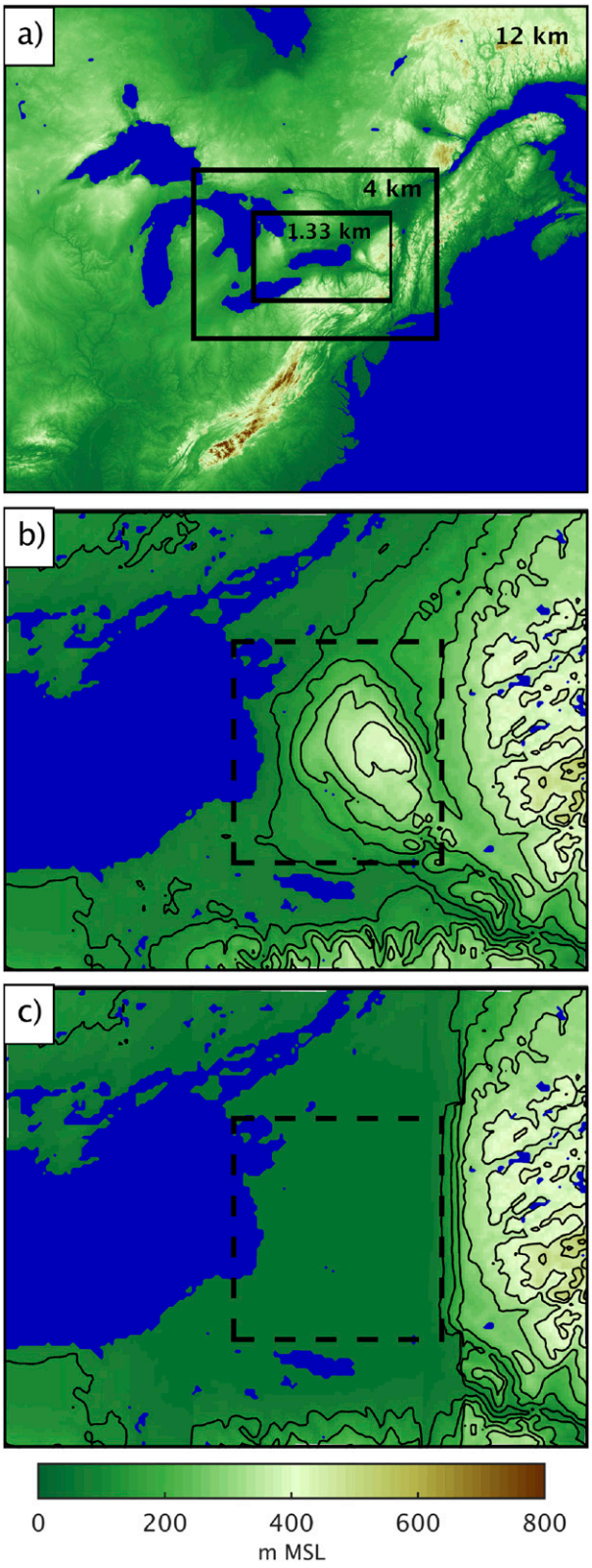

FIG. 2. (a) WRF domains with real topography (m MSL, color filled following scale at bottom). (b) Control 1.33-km topography [m MSL, as in (a)] in the Tug Hill region. Dashed lines indicate microphysics study volume. (c) As in (b), but for NoTug.

empirically derived power-law relationship between precipitation rate and KTYX radar reflectivity (i.e., Z–S relationship), a technique described by Wüest et al. (2010), to disaggregate 6-h manual precipitation measurements to higher temporal resolution and estimate precipitation at SC and NR during periods that do not align with the 6-h manual measurement times. Three mobile X-band radars were operated by the Center for Severe Weather Research along the Lake Ontario shoreline during IOP2b, but data quality was poor over Tug Hill so the data are not used in this study. The University of Wyoming King Air (UWKA) research aircraft also collected transects of W-band cloud radar data across the lake-effect system for ~2.5 h during IOP2b. We do not examine the W-band cloud radar dataset here, but direct the reader to Welsh et al. (2016) for a multiradar analysis of IOP2b and to Bergmaier et al. (2017) for an analysis of the secondary circulation within the lake-effect system, as well as a comparison of the UWKA cloud radar data with the WRF simulations described in this paper.

b. *WRF simulations*

We used the Advanced Research version of the WRF Model, version 3.7 (WRF-ARW; Skamarock and Klemp 2008; hereinafter WRF) to produce numerical simulations of OWLeS IOP2b. We configured all simulations using three one-way nested domains with 12-, 4-, and 1.33-km grid spacing (Fig. 2a), 36 terrain-following half-η levels with the highest resolution within the boundary layer, and a 5000-m-deep Rayleigh damping layer at the upper boundary. We performed a series of sensitivity studies using various microphysics, radiation, and planetary boundary layer and surface layer schemes (not shown). Based on the combination that best captured the observed precipitation distribution and taking into account microphysics and planetary boundary layer/surface layer sensitivity studies for lake-effect events presented in Reeves and Dawson (2013), McMillen and Steenburgh (2015a), and Conrick et al. (2015), the simulations presented in this paper use the Thompson cloud microphysics (Thompson et al. 2008), Rapid Radiative Transfer Model longwave radiation (Iacono et al. 2008), Dudhia shortwave radiation (Dudhia 1989), Yonsei University planetary boundary layer (Hong et al. 2006), revised MM5 surface layer (Jiménez et al. 2012), and Noah land surface model (Chen and Dudhia 2001) parameterizations. The Kain–Fritsch 2 cumulus parameterization (Kain 2004) was used in the 12-km domain only.

All simulations were cold-start initialized at 1200 UTC 10 December 2013 and run until 0600 UTC 12 December 2013 (all subsequent dates are in 2013 unless otherwise

specified). We used the U.S. Geological Survey (USGS) land-use dataset for land-use characteristics and the North American Mesoscale Forecast System (NAM) analyses for atmospheric initial and lateral boundary conditions (6-h intervals), land surface conditions, and snow-coverage distribution.

Over the Great Lakes, we specified ice cover manually based on inspection of Great Lakes Environmental Research Laboratory (GLERL) ice-cover analyses from 11 and 12 December and included localized ice cover in Black Bay on Lake Superior, Green Bay on Lake Michigan, and Saganaw Bay on Lake Huron (not shown). Far western Lake Erie was predominantly ice free on 11 December but developed 95% ice coverage by 12 December. We elected to keep this area ice free as the event ended late on 11 December. Lake Ontario was nearly ice free during the study period except for spotty ice confined to the north shore near Prince Edward and localized ice cover in Henderson and Chaumont Bays. In the 1.33-km domain we allowed for some coverage of ice in these bays, but otherwise kept Lake Ontario ice free. We also allowed for some coastal ice in portions of Georgian Bay.

Over smaller bodies of water, a lack of operational ice-cover analyses combined with extensive cloud cover in the days around IOP2b made it difficult to assess ice conditions. Based on inspection of Moderate Resolution Imaging Spectroradiometer (MODIS) imagery in cloud-free areas during the days preceding and following the event, we classified most small bodies of water as ice covered. Exceptions include Lakes St. Claire and Simcoe, where ice was specified along the shores, the Finger Lakes, the Niagara River, the St. Lawrence River, and Lake Champlain.

For lake-surface temperatures (LSTs) over the Great Lakes, we used 6-h analyses from the GLERL Great Lakes Coastal Forecasting System. We set the open water of the smaller bodies of water noted above to 0°C with the exceptions of Lake Simcoe, whose NAM-derived LST seemed appropriate (above 0°C, but colder than the nearby Great Lakes), and the Finger Lakes, which we set to 2°C except for Seneca Lake, which we set to 4°C based on the climatology of Laird et al. (2010).

We present two simulations in this paper: Control, which was run using the configuration described above, and NoTug, which is identical to Control except that we reduced the elevation of Tug Hill to the mean elevation of the surrounding lowlands in all three domains (cf. Figs. 2b and 2c for comparison of the terrain in the 1.33-km domains). Land surface characteristics such as land use, snow cover, and vegetation were retained where the terrain was modified. However, the WRF preprocessing system adjusted the soil temperature, soil moisture, and skin temperature based on elevation and replaced the atmosphere that Tug Hill previously occupied by assuming a moist-adiabatic lapse rate and using winds from the lowest model level in the NAM initial conditions. Given the relatively small size of Tug Hill, the 6–9-h integration time before the start of lake-effect precipitation, and the consistently similar large-scale conditions in Control and NoTug at all simulation times, we find it reasonable to attribute the differences between the two runs to changes in orography.

3. Event overview and model validation

The evolution of synoptic conditions and lake-effect precipitation during OWLeS IOP2b is described in detail in Campbell et al. (2016), but we summarize it here. Two shortwave troughs embedded in a broad 500-hPa trough moved through the Great Lakes region from 10 to 12 December, influencing lake-effect precipitation over and downstream of all the Great Lakes. IOP2b sampled the periods of heaviest lake-effect precipitation over and east of Lake Ontario from 2300 UTC 10 December to 0200 UTC 12 December (Kristovich et al. 2017). During this period, the LLAP system fluctuated between nonbanded and banded modes, and settled along the major axis of Lake Ontario beginning at ~0300 UTC [e.g., Figs. 3a,c,e; see also Campbell et al. (2016)]. A strong band that developed at ~1745 UTC 11 December (e.g., Fig. 3e) generated the largest precipitation accumulation rates over Tug Hill before the LLAP system moved southward after ~2200 UTC 11 December. To focus on the effects of Tug Hill, we examine the period from 0300 to 2200 UTC 11 December when the LLAP system was well developed, oriented along the major axis of the lake, and produced persistent snowfall over Tug Hill. This period captures 78% (85%) of the radar-disaggregated precipitation that fell at SC (NR) during the 24-h period (0000 UTC 11 December–0000 UTC 12 December) examined by Minder et al. (2015) and Campbell et al. (2016).

The radar-derived precipitation distribution for 0300–2200 UTC 11 December features a narrow band that broadens and reaches a maximum over Tug Hill (Fig. 4a). Radar-disaggregated precipitation totals from this period increase from 28.5 mm at SC near the base of Tug Hill to 48.9 mm at NR on the western slope, just upstream of the radar-derived precipitation maximum. Over Tug Hill, the radar-derived precipitation band shifts orientation by ~15° so that it extends east-northeastward into the Adirondack Mountains. As a result, the precipitation maximum over the western

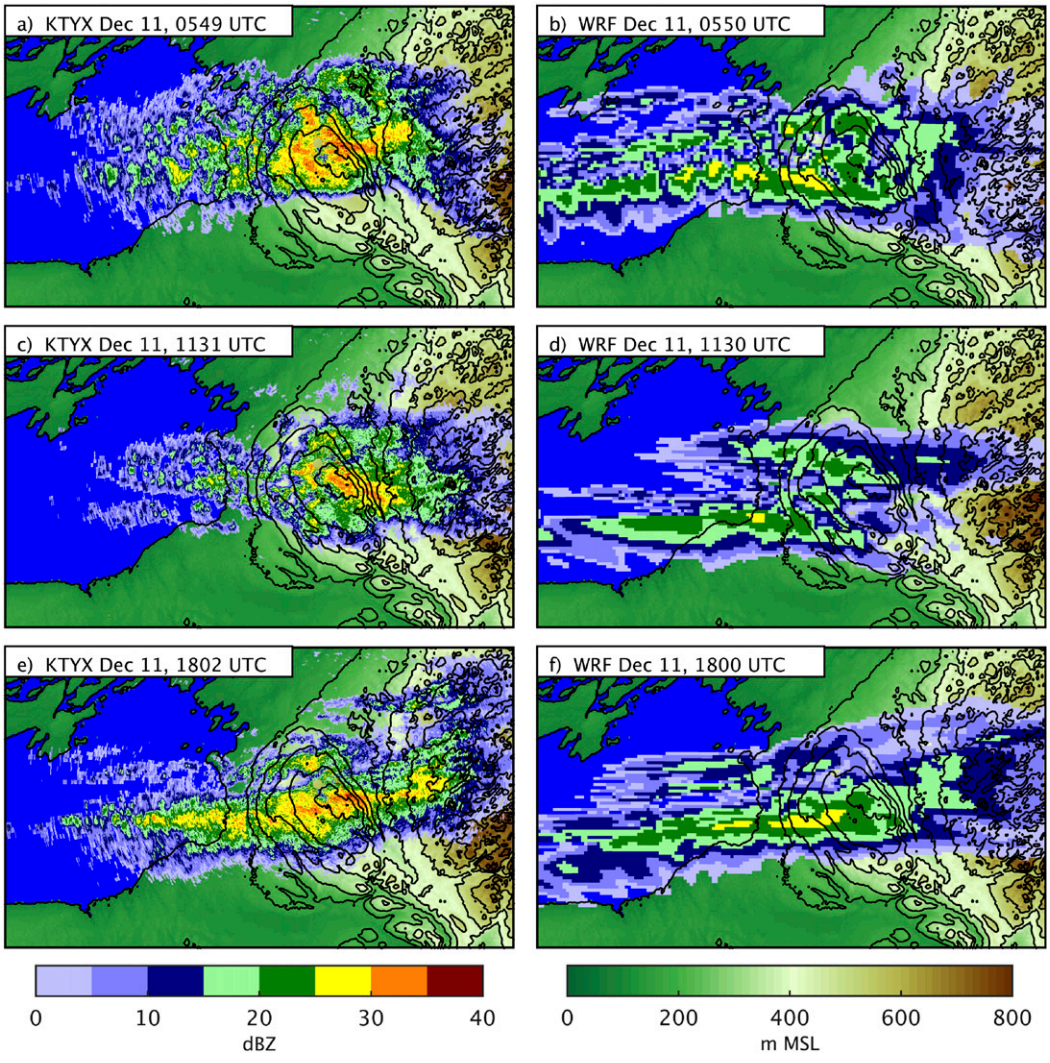

FIG. 3. (a) KTYX 0.5° radar reflectivity (dBZ, color filled following scale at bottom left) and topography (m MSL, contoured every 100 m and color filled following scale at bottom right) at 0549 UTC. (b) WRF seventh-half-η-level reflectivity [dBZ, as in (a)] and topography [m MSL, as in (a)] at 0550 UTC. (c),(d) As in (a),(b), but for 1131 and 1130 UTC, respectively. (e),(f) As in (a),(b), but for 1802 and 1800 UTC, respectively.

Adirondack Mountains is ~15 km north of the precipitation maximum over Tug Hill.

The precipitation produced by Control during this period compares well to the radar-derived precipitation, although the simulated maximum does not broaden as much over Tug Hill (cf. Figs. 4a,b). Compared to the radar-disaggregated precipitation, Control underpredicts precipitation at SC by 36.4% (20.9 mm) and overpredicts at NR by 12.9% (55.2 mm), resulting in a larger orographic ratio (NR precipitation/SC precipitation; 2.6) than obtained from radar disaggregation (1.7). A slight southward band positioning bias in Control (cf. Figs. 4a,b) causes the underprediction at SC and contributes to the larger orographic ratio. The orographic ratio along the axis of the simulated band is 1.6, which compares well to the observed. At individual time steps, Control produces physically realistic lake-effect features, however, it generates banded organizational modes more frequently than observed (cf. Figs. 3a,c,e and 3b,d,f). McMillen and Steenburgh (2015b) document a similar banded-mode bias in WRF simulations of lake effect over the Great Salt Lake. There are also differences in the timing and/or position of precipitation features, as is common in numerical simulations of lake-effect systems (e.g., Steenburgh and Onton 2001; Ballentine and Zaff 2007; Arnott 2010; Shi et al. 2010; Theeuwes et al. 2010; Alcott and Steenburgh 2013; Reeves and Dawson 2013; McMillen and

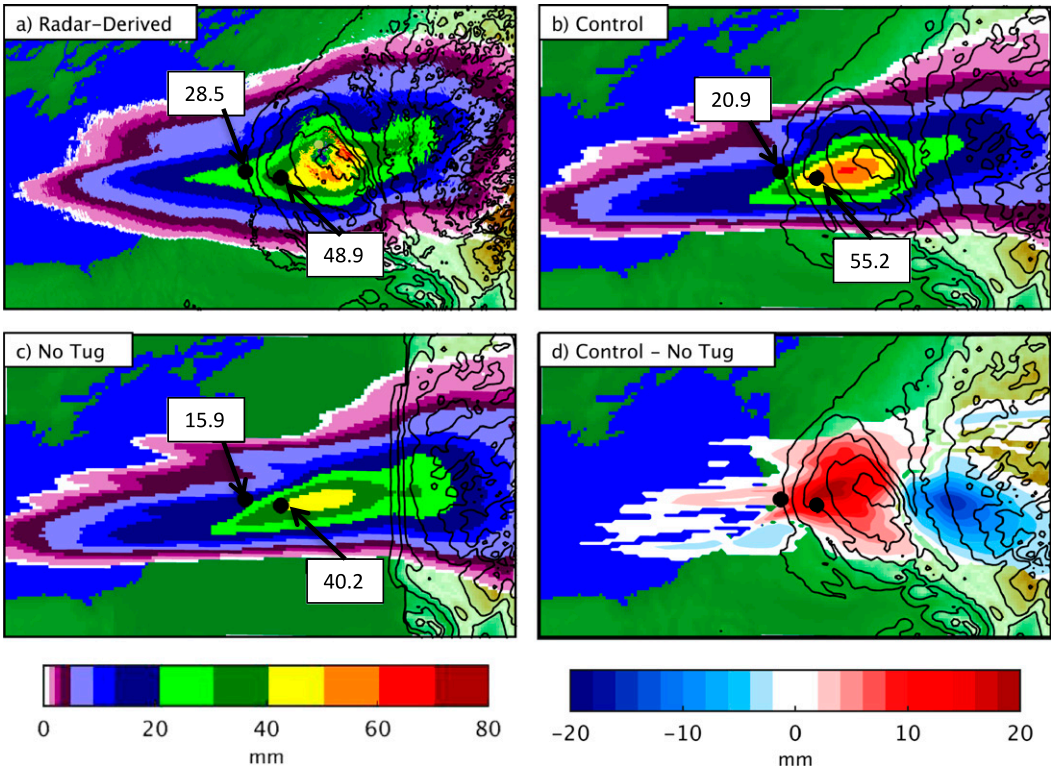

FIG. 4. (a) Radar-derived precipitation (mm, color filled following scale at bottom left) from 0300 to 2200 UTC 11 Dec with radar-disaggregated precipitation at SC and NR annotated. (b) Control precipitation [as in (a)] with simulated precipitation (mm) at SC and NR annotated. (c) As in (b), but for NoTug. (d) The precipitation difference between Control and NoTug (mm, color filled following scale at bottom right), and Control topography (m MSL, contoured every 100 m and color filled following scale in Fig. 2).

Steenburgh 2015b). Nevertheless, accounting for the slight southward bias in the band position, the simulated precipitation is a reasonable match to radar-derived and radar-disaggregated precipitation and we conclude that Control captures the spatial distribution of precipitation and the broader effects of Tug Hill.

4. Land-breeze fronts

Control produces two quasi-stationary land-breeze fronts[1] that develop along and extend downstream from the southern and southeastern shorelines of Lake Ontario. The first land-breeze front (LBF1) forms along a bulge in the southern shoreline between St. Catharines, Ontario, and Thirty Mile Point, New York (Fig. 5a; for locations see Fig. 1). The band of boundary layer (1000 m MSL) ascent that surmounts LBF1 extends downstream across Lake Ontario to the eastern shoreline (Fig. 5b) and plays a primary role in LLAP-system development over Lake Ontario. The second land-breeze front (LBF2) forms along the southeast shoreline of the lake and extends northeastward and inland across Tug Hill, cutting obliquely across the LLAP system (Fig. 5a, see Fig. 2 for LLAP-system orientation). As described by Steenburgh and Campbell (2017), each land-breeze front represents a boundary between lake-modified and continental air, with the shoreline geometry and direction of the incident flow relative to the coastline playing important roles in their genesis and evolution. Time-mean boundary layer ascent is especially strong where LBF2 extends downstream over Tug Hill and cuts obliquely across the LLAP system (Fig. 5b). A third band of time-mean ascent is also found farther north along a weaker airmass boundary that extends downstream from Point Petre.

Trajectories calculated using three-dimensional grid-resolved winds at 10-min time steps illustrate how differing parcel paths and thermodynamic histories lead to the inland extension of LBF2 over Tug Hill. Trajectories

[1] Although typically used to describe the leading edge of cool, dense, offshore flow at night, we use the term land-breeze front here because it has been used previously to describe airmass boundaries during lake-effect storms that are generated by differential surface heating. For further discussion, see Steenburgh and Campbell (2017).

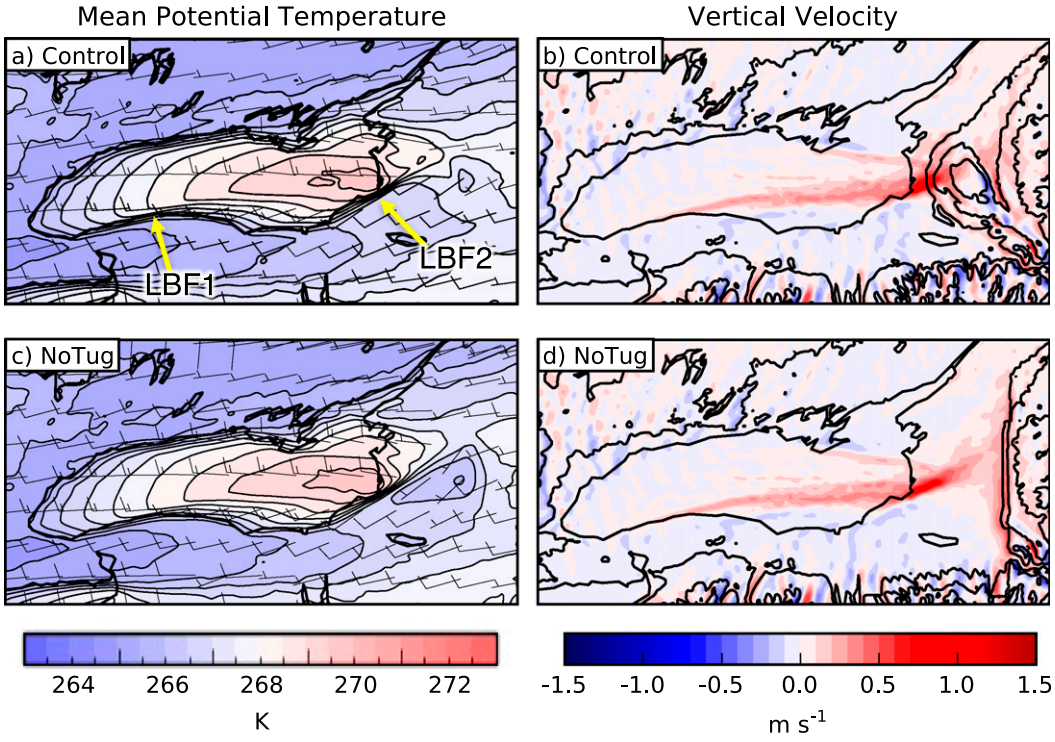

FIG. 5. (a) Control time-mean (0300–2200 UTC 11 Dec) lowest-half-η-level potential temperature (K, contoured every 0.5 K and color filled following scale at bottom left) and wind barbs (full and half barb denote 5 and 2.5 m s^{-1}, respectively). (b) Control time-mean (0300–2200 UTC 11 Dec) 1000-m MSL vertical velocity (m s^{-1}, shaded following color scale at bottom right) and topography (m MSL, contoured every 150 m). (c),(d) As in (a),(b), but for NoTug. Potential temperature and vertical velocity smoothed using a seven-point spectral cowbell filter (Barnes et al. 1996).

ending on the lowest-half-η level at 1800 UTC[2] along transect A–A′, which stretches across the lowlands upstream of Tug Hill, cluster into three major categories (Fig. 6a). The first category includes the red trajectories that traverse the length of Lake Ontario in predominantly westerly flow and terminate immediately north of LBF2 (Fig. 6a). These trajectories feature higher potential temperatures due to warming over Lake Ontario (Figs. 6a,b), preconditioning by upstream Lake Huron (not shown), and/or a more elevated origin. The latter is reflected in the red trajectory that experiences little potential temperature change as it is relatively elevated over Lake Ontario but ultimately descends to the surface within a grid-resolved downdraft. In contrast, there are other trajectories removed from the surface within grid-resolved updrafts over eastern Lake Ontario (not shown). This represents a vertical scrambling of the lake-modified air mass, similar to that which occurs during airmass transformation within orographic precipitation systems (Smith et al. 2003). The second category includes the blue trajectories that move through the land bridge between Lakes Erie and Ontario and circumscribe Lake Ontario through the lowlands to the south. These trajectories, which terminate on the south side of LBF2, warm by ~3 K due to daytime heating but remain colder than the red trajectories. The third category includes the orange trajectories that follow the north shoreline of Lake Ontario and move across the northeast portion of the lake. These trajectories have higher potential temperatures than those south of LBF2 when they enter the Lake Ontario region, due to prior modification by Lake Huron and/or a more elevated origin, and are further modified over northern and northeastern Lake Ontario. Farther inland, along transect C–C′, the orange trajectories remain ~1–2 K warmer than the blue trajectories to the south (Figs. 6c,d). The lack of red trajectories along C–C′ reflects the lifting and ascent over LBF2 of low-level air that has traversed Lake Ontario. Thus, inland and over Tug Hill, LBF2 separates air that

[2] We present 1800 UTC because it is during the period of strongest precipitation over Tug Hill, but note that the thermal contrasts across LBF2 are weaker at this time than earlier in IOP2b because of daytime surface heating over land.

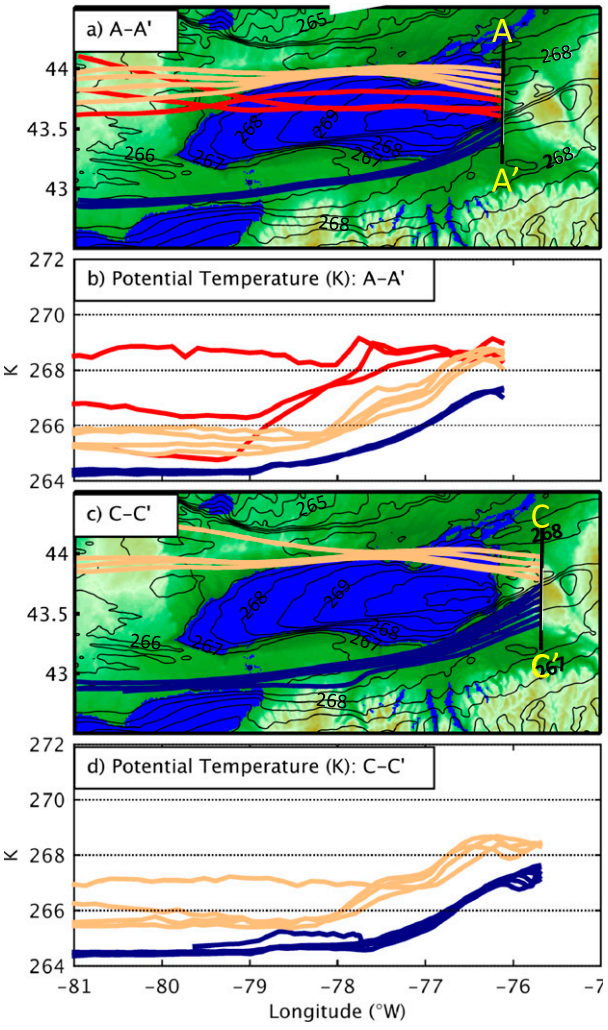

FIG. 6. (a) Control trajectories ending at the lowest-half-η level along transect A–A′ (colored lines), lowest-half-η-level potential temperature (contoured every 0.5 K), and topography (m MSL, color filled following scale in Fig. 2) at 1800 UTC 11 Dec. Potential temperature smoothed using a seven-point spectral cowbell filter (Barnes et al. 1996). (b) Potential temperature along trajectories in (a). (c) As in (a), but for trajectories ending along transect C–C′. (d) As in (b), but along trajectories in (c).

traversed the north shoreline and moved across northeast Lake Ontario from cooler air that passed through the lowlands south of Lake Ontario, avoiding lake modification.

Observations collected over and around Tug Hill during IOP2b confirm the presence of LBF2. At NR, the wind shifted between westerly and southwesterly several times during IOP2b (Fig. 7a). When the surface winds were westerly (peach shading), the wind speed hovered at ~6 m s^{-1}, relative humidity was at ~97%, and temperature was at ~−6°C (Figs. 7a,b). In contrast, when the surface winds were southwesterly (blue shading), the wind speed, relative humidity, and temperature were consistently lower (~3 m s^{-1}, ~95%, and ~−8°C, respectively). After ~1700 UTC, these thermal and directional contrasts lessen because of daytime heating but are still apparent. These fluctuations are consistent with the southwest–northeast-oriented LBF2 moving back and forth across NR and demonstrate a similar temperature contrast (~2°C) as produced by Control.

Soundings launched at NR also confirm the presence of LBF2. When LBF2 was north of NR, observed soundings (black lines and wind barbs) reveal a shallow layer of relatively cold air surmounted by a stable layer ~50 hPa above the surface (Figs. 8a,c; blue shading). Surface winds in the shallow layer of cold air were southwesterly, but veered with height to westerly through the stable layer. In contrast, observed soundings launched when LBF2 was south of NR featured westerly winds and ~1°–2°C higher near-surface temperatures (Fig. 8b; peach shading). The colder air mass south of LBF2 is also evident in simulated soundings from Control at NR (red lines and wind barbs), with a shallow layer of cold air surmounted by a stable layer at all times (Figs. 8a–c). In Control, however, LBF2 remains just north of NR, so that a shift to westerly low-level flow and associated warming does not occur as observed at 1141 UTC (Fig. 8b). The Control soundings also reveal a stronger capping stable layer or inversion than observed near 700 hPa, with a weak cold bias below this level in some soundings, indicating a slightly more stable air mass below the capping inversion than observed. Wind directions and speeds are realistically simulated.

5. Influence of land-breeze front over Tug Hill

A zonal time-mean cross section, oriented roughly parallel to the large-scale flow along Lake Ontario, reveals the shallow nature of the cool southwesterly flow and the influence of LBF2 over Tug Hill (Fig. 9a). Westerly flow from over Lake Ontario rises over the layer of cold air behind LBF2 (surface position of LBF2 denoted by red arrow), resulting in an ascent maximum over LBF2 and a lofted hydrometeor mixing ratio maximum that arcs to the surface farther inland and downstream over Tug Hill. A series of meridional time-mean cross sections taken from the eastern Lake Ontario shoreline to Tug Hill provide another view of this inland transition (Fig. 10). Near the coast, along cross section A–A′, LBF2 features a well-defined nose, with a tongue of cooler air to the south that extends to ~750 m MSL (Fig. 10a, surface position of LBF2 denoted by red arrow). A strong time-mean ascent and hydrometeor mixing ratio maximum is roughly collocated with LBF2,

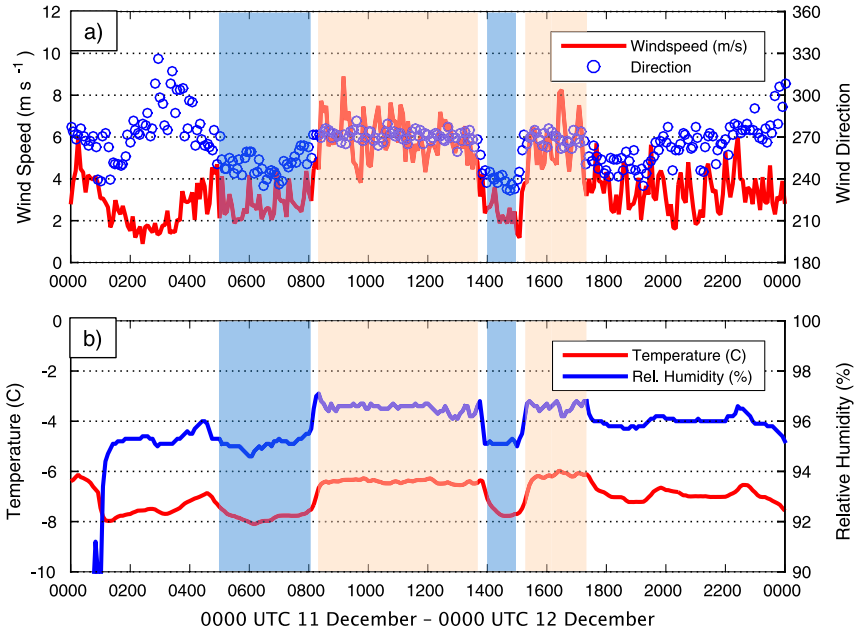

FIG. 7. (a) Observed wind speed (red line) and wind direction (blue circles) at NR. (b) Observed temperature (red line) and relative humidity (blue line). Blue (peach) shading indicates periods when LBF was north (south) of NR.

and reflects the downstream extension of the lake-effect system that formed along LBF1, as well as the influence of LBF2. A pronounced secondary circulation is visible in the cross-section-parallel wind vectors, with convergence near the surface and divergence aloft [this circulation is likely enhanced by latent heating within the lake-effect system, as discussed by Bergmaier et al. (2017)]. A weaker ascent and hydrometeor mixing ratio maximum is found along a secondary airmass boundary at ~43.8°N and is associated with the convergence and ascent that extend downstream from Pt. Petre (Steenburgh and Campbell 2017).

Over Tug Hill, along cross sections B–B′ (Fig. 10b) and C–C′ (Fig. 10c), LBF2 is shallower (this partially reflects the higher surface elevation) and farther north than along A–A′, consistent with its oblique orientation

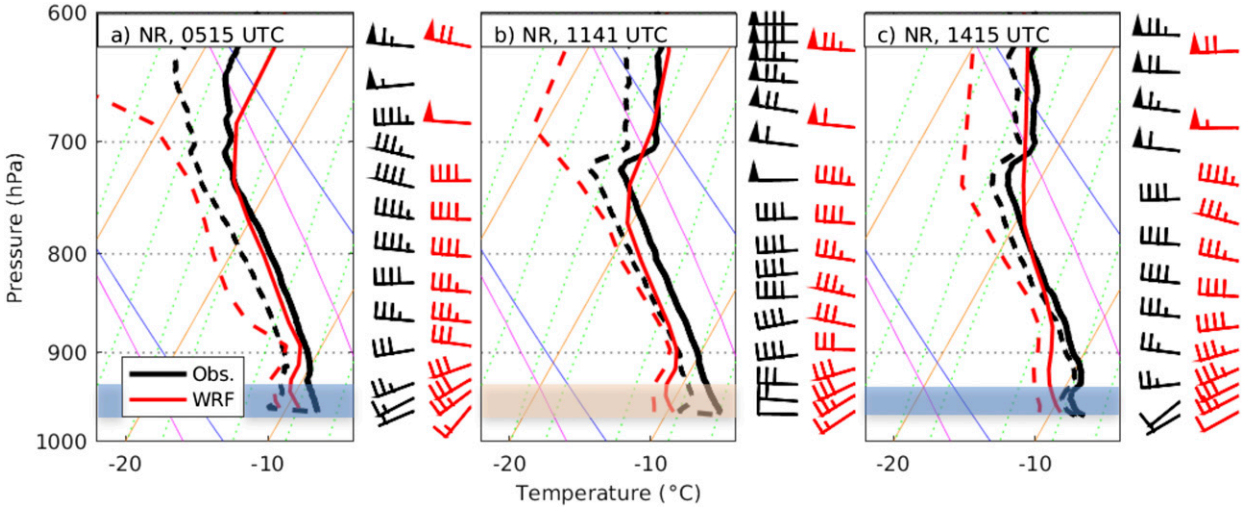

FIG. 8. Observed (black) and Control (red) skew T–log$p$ diagrams [temperature (solid line), dewpoint (dashed line), and wind barbs (full and half barbs denote 5 and 2.5 m s^{-1}, respectively)] at NR at (a) 0515, (b) 1141, and (c) 1415 UTC 11 Dec. Control soundings are the closest 10-min interval to the observed sounding time. Blue (peach) shading indicates periods when LBF was north (south) of NR.

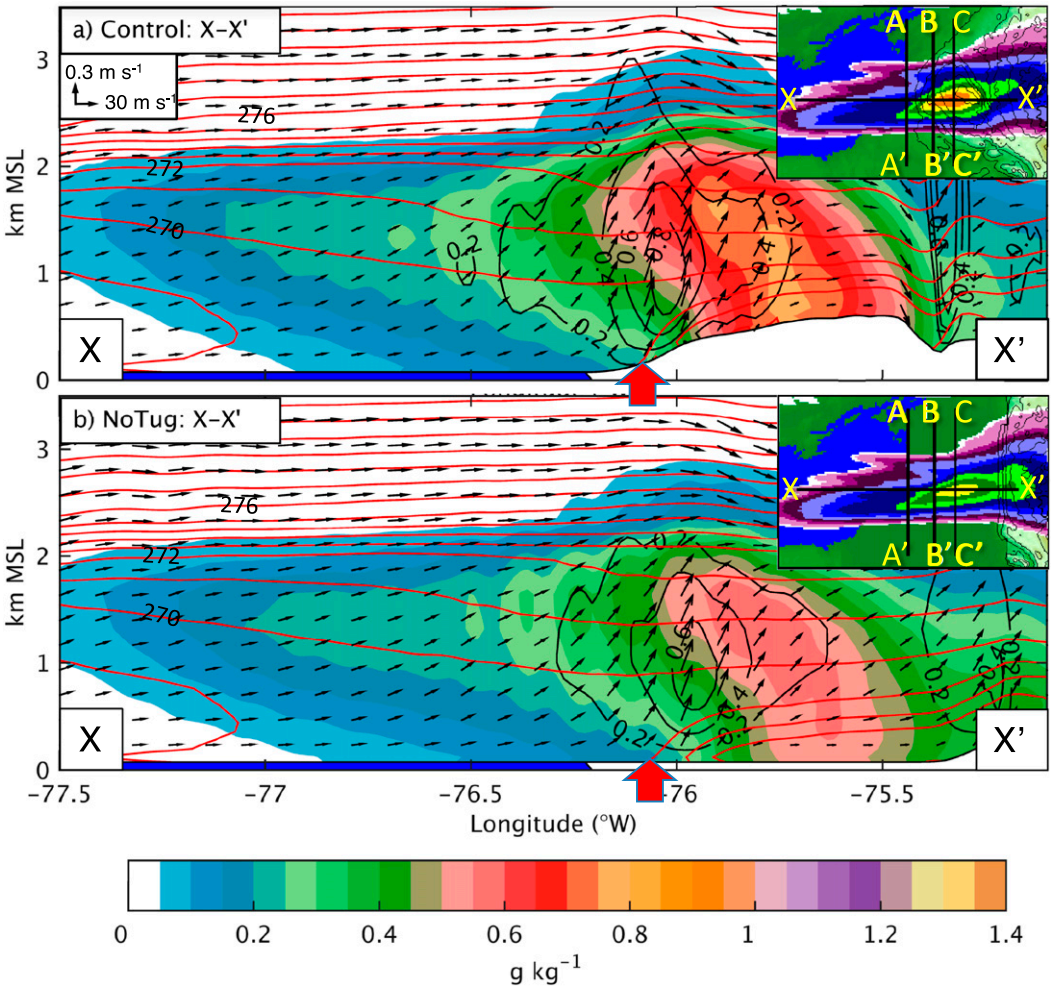

FIG. 9. (a) Control time-mean (0300–2200 UTC 11 Dec) hydrometeor mixing ratio (g kg^{-1}, color filled following scale at bottom), potential temperature (red contours every 1 K), vertical velocity (positive-only black contours every 0.2 m s^{-1}), and cross-section-parallel wind vectors [components are zonal wind u and vertical velocity w, scaled as in inset in (a)] along X–X′ and averaged across five grid points in the cross-plane direction. Red arrow indicates surface position of LBF2. Inset shows cross-sectional locations and Control precipitation from 0300 to 2200 UTC. (b) As in (a), but for NoTug.

relative to the lake-effect system. A time-mean ascent maximum continues to surmount LBF2, but weakens and broadens from A–A′ to C–C′ (cf. Figs. 10a–c). This inland transition is consistent with UWKA cloud radar observations of a weakened primary updraft but continued secondary circulation in transects over Tug Hill (Bergmaier et al. 2017). Concurrently, the hydrometeor mixing ratio maximum strengthens, broadens, and shifts downward toward the surface, indicative of the growth, transport, and fallout of hydrometeor mass. Larger ($\gtrsim$0.25 g kg^{-1}) hydrometeor mixing ratios cover a greater area at the surface over Tug Hill, consistent with a broadening of the LLAP system.

The land-breeze fronts and associated vertical velocity maxima produced in Control are also produced in NoTug, including the strong ascent maximum where LBF2 cuts obliquely across the LLAP system (cf. Figs. 5a,b and 5c,d). NoTug also produces a vertical velocity maximum over LBF2 and an arcing and descending hydrometeor mixing ratio maximum due to downstream transport and fallout (cf. Figs. 9a,b). Finally, NoTug produces a precipitation maximum in roughly the same location as in Control, albeit one that is weaker and narrower (cf. Figs. 4b,c). These similarities suggest that LBF2 is an important contributor to the IOP2b Tug Hill precipitation maximum, which is produced in NoTug even in the absence of orographic uplift.

The oblique orientation of LBF2 relative to the LLAP system contributes to a broadening and shift in

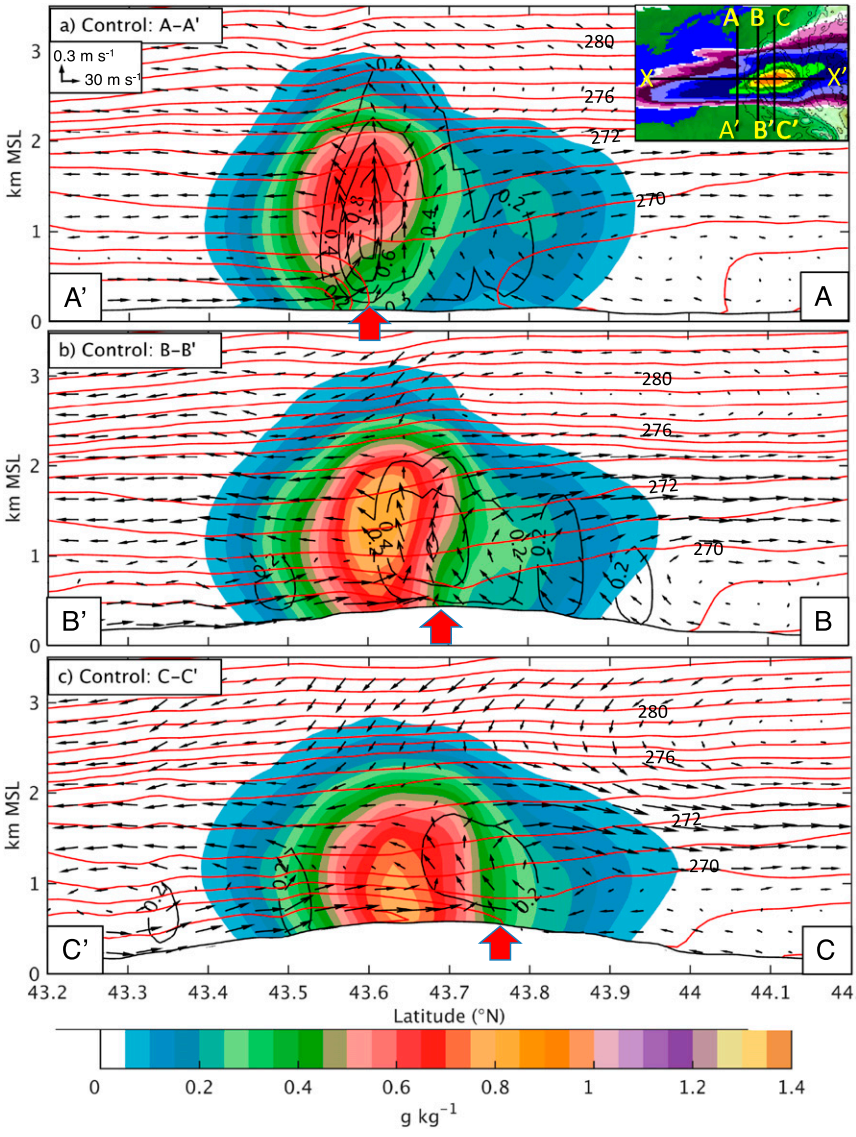

FIG. 10. As in Fig. 9a, but for cross sections (a) A–A′, (b) B–B′, and (c) C–C′, and vectors as in scale in inset in (a).

orientation of the precipitation band over Tug Hill. In particular, the orientation of strong ascent along LBF2 in both Control and NoTug (Figs. 5b,d) is consistent with the northward expansion of the precipitation band over Tug Hill and its east-northeastward extension into the western Adirondack Mountains. The expansion and orientation shift occur because ascent along LBF2 serves as a locus for hydrometeor generation and growth, as discussed earlier, and also influences hydrometeor fallout and transport, which is illustrated by hydrometeor trajectories ending along the 1-h precipitation maximum at 1800 UTC (Fig. 11). These hydrometeor trajectories use three-dimensional grid-resolved winds at 10-min intervals, but the vertical velocity component includes an average hydrometeor fall speed weighted by the mixing ratio of each hydrometeor type (i.e., snow, rain, and graupel, although snow predominates). In Control, hydrometeors that end within the banded precipitation maximum at 1800 UTC pass through the ascent maximum along LBF2 (at ~1.0–2.0 km MSL), are temporarily lofted, and are subsequently transported ~20 km eastward, turning to the northeast in the near-surface southwesterly flow (Figs. 11a,c, red circle identifies region of lofting). Similarly, hydrometeor trajectories farther north along and downstream of the LBF2 ascent maximum follow similar paths (not shown), as do hydrometeor trajectories in NoTug (Figs. 11b,d). Thus, LBF2 contributes not only to

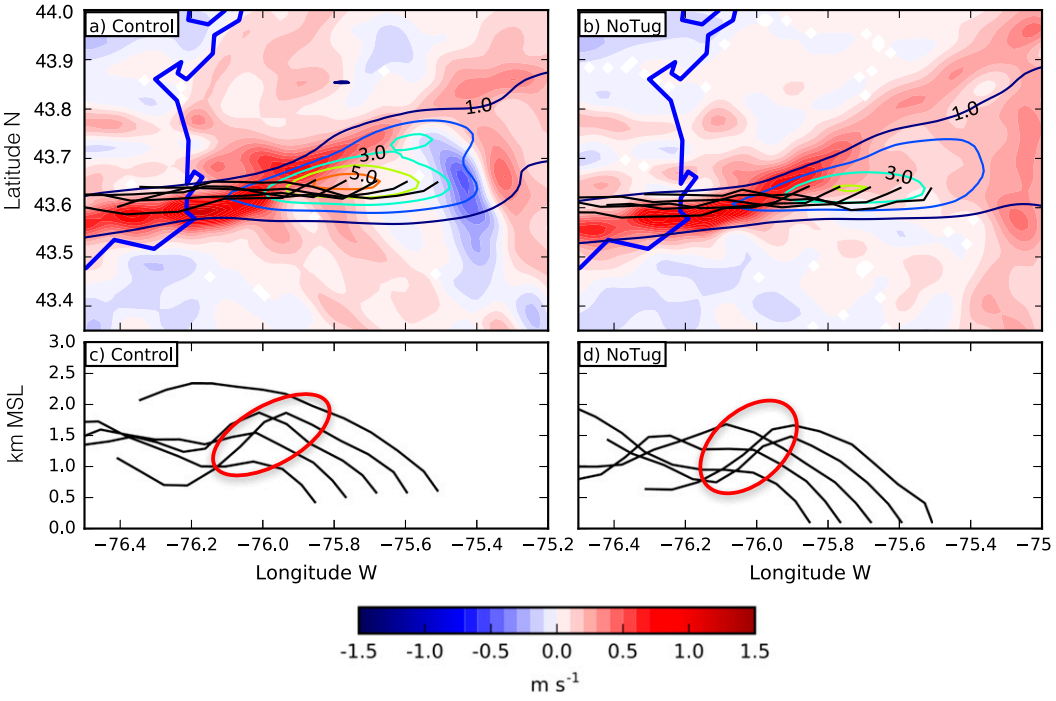

FIG. 11. (a) Control 1000-m MSL vertical velocity (m s^{-1}, color filled following scale at bottom), 1-h accumulated precipitation (mm, contoured at 1-mm intervals), and hydrometeor trajectories (black lines) ending on the lowest-half-η level at 1800 UTC 11 Dec. Blue lines indicate shorelines. Vertical velocity and precipitation smoothed using a seven-point spectral cowbell filter (Barnes et al. 1996). (b) As in (a), but for NoTug. (c) Height of trajectories in (a). Red oval denotes region of ascent along LBF2. (d) As in (c), but for trajectories in (b).

the Tug Hill precipitation maximum, but also to its broadening and orientation shift.

6. Orographic enhancement mechanisms

A plot of the difference in precipitation between the two simulations reveals a broad region over Tug Hill in which precipitation is greater in Control (Fig. 4d), as well as a stronger decrease in precipitation in the lee of Tug Hill, both of which reflect orographic influence. Control and NoTug both produce LBF2 and an associated precipitation maximum, however in Control, the ascent maximum along LBF2 is stronger and wider (cf. Figs. 5b,d). A difference plot between the Control and NoTug time-mean vertical velocities at 1000 m MSL shows that Control produces a boomerang-shaped region of ascent around the convex windward slope of Tug Hill and a narrow band of subsidence to the lee that is strongest over the southern and central lee slopes (Fig. 12). The boomerang-shaped region of ascent is similar to that produced in idealized simulations of flow interacting with a convex ridge (Watson and Lane 2012). The difference in ascent between the two runs maximizes just upstream of Tug Hill and along LBF2. A slight northwestward shift in the position of LBF2 in Control compared to NoTug only partially accounts for this difference (as well as the southwest–northeast-oriented negative difference just to the south, Fig. 12). Thus, the boomerang-shaped region of orographic ascent enhances precipitation along LBF2 and contributes

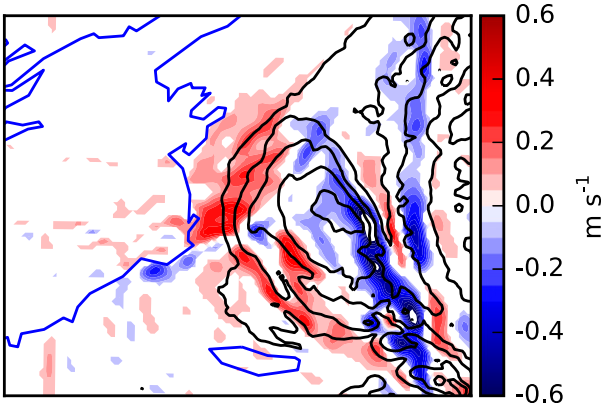

FIG. 12. Difference between Control and NoTug time-mean (0300–2200 UTC 11 Dec) 1000-m vertical velocity (m s^{-1}, following scale at right) with Control topography (m MSL, contoured every 100 m). Blue lines indicate shorelines. Vertical velocity smoothed using a seven-point spectral cowbell filter (Barnes et al. 1996).

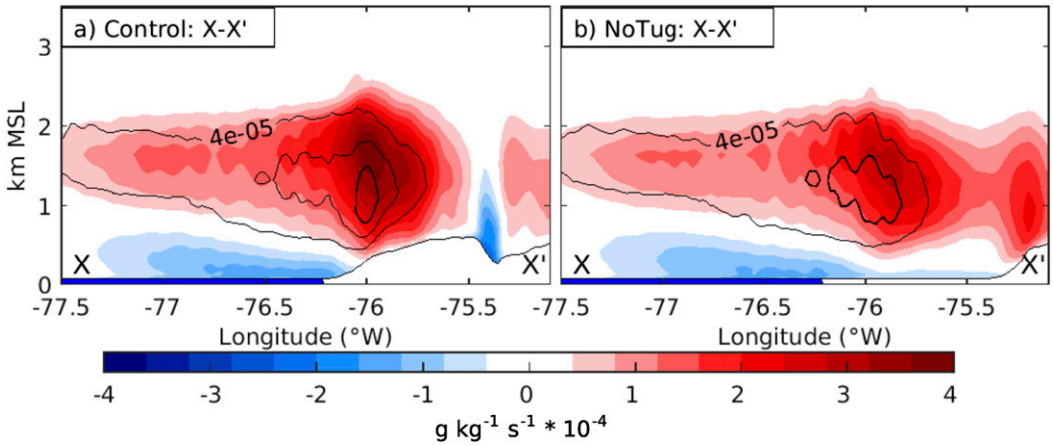

FIG. 13. Control time-mean (0300–2200 UTC 11 Dec) hydrometeor mass tendencies from deposition (g kg^{-1} s^{-1}, following red shading at bottom), accretion (contours every 4×10^{-5} g kg^{-1} s^{-1} beginning at 4×10^{-5} g kg^{-1} s^{-1}), and sublimation (g kg^{-1} s^{-1}, following blue shading at bottom) along cross section X–X′ and averaged across five grid points in the cross-plane direction. (b) As in (a), but for NoTug.

to a broadening of the precipitation region over Tug Hill. Downstream of Tug Hill, the greater decline in precipitation and stronger northward shift in the precipitation band in Control compared to NoTug reflects the influence of subsidence over the southern and central lee slopes.

Since orographically induced ascent has an impact on hydrometeor generation and growth, we now turn our attention to the parameterized production and mass growth tendencies of hydrometeor mass within a study volume encompassing the area east of Lake Ontario (see Figs. 2b and 2c for location). The simulated time-mean total hydrometeor mixing ratio (including snow, rain, and graupel) in both the Control and NoTug study volumes is 99.9% snow and 0.1% graupel. Graupel is primarily produced in isolated convective pockets concentrated over the lake and near the coast in both simulations (not shown), consistent with surface-based and aircraft observations during IOP2b, which documented only occasional graupel or heavily rimed crystals (e.g., Minder et al. 2015; Welsh et al. 2016). Because of the negligible contribution of graupel and rain to the total hydrometeor mixing ratio in the study volume, we focus our analysis on snow.

The primary snow mass growth terms within the study volume are vapor deposition to snow [hereafter deposition; accounts for 82.4% (80.1%) of hydrometeor mass growth within the Control (NoTug) study volume] and snow collecting cloud liquid water [hereafter accretion; accounts for 17.4% (19.7%) of hydrometeor mass growth within the Control (NoTug) study volume]. In Control, time-mean cross sections along X–X′ show lofted maxima of depositional and accretional mass growth, roughly collocated with or just downstream of the orographically enhanced ascent maximum along LBF2, that extend downstream over Tug Hill (Figs. 9a and 13a). Although also evident in NoTug, these maxima are clearly stronger in Control (cf. Figs. 13a,b). Plan-view difference plots at 1000 m MSL show that the larger depositional growth in Control occurs near and downstream of the boomerang-shaped region of ascent over the convex windward slopes of Tug Hill (cf. Figs. 12 and 14a), which contributes to a strengthening and broadening of the precipitation maximum over Tug Hill. In contrast, differences in accretion, which makes up a smaller proportion of the total mass growth tendency, are aligned along LBF2 (Fig. 14b). Although partly related to LBF2 positioning differences, the largest difference in accretion between Control and NoTug occurs along LBF2 upstream of Tug Hill. Therefore, the stronger ascent upstream of Tug Hill in Control increases accretion rates along LBF2, further enhancing the Tug Hill precipitation maximum. The increase in accretion along LBF2 does not, however, significantly broaden the precipitation maximum.

Contrasts in low-level sublimation also contribute to the larger Tug Hill precipitation maximum in Control compared to NoTug. In Control, sublimation, which occurs primarily below cloud base, accounts for a 28.4% decrease in total hydrometeor mass within the study volume compared to 39.6% in NoTug. In Control, sublimational losses are largest over Lake Ontario and the coastal lowlands and decrease over the windward slopes of Tug Hill where orographic ascent increases relative humidity (not shown) and enhances hydrometeor growth and precipitation rates (Figs. 4d and 13). The sublimational losses then reach a minimum over the upper reaches of Tug Hill, which extends above cloud

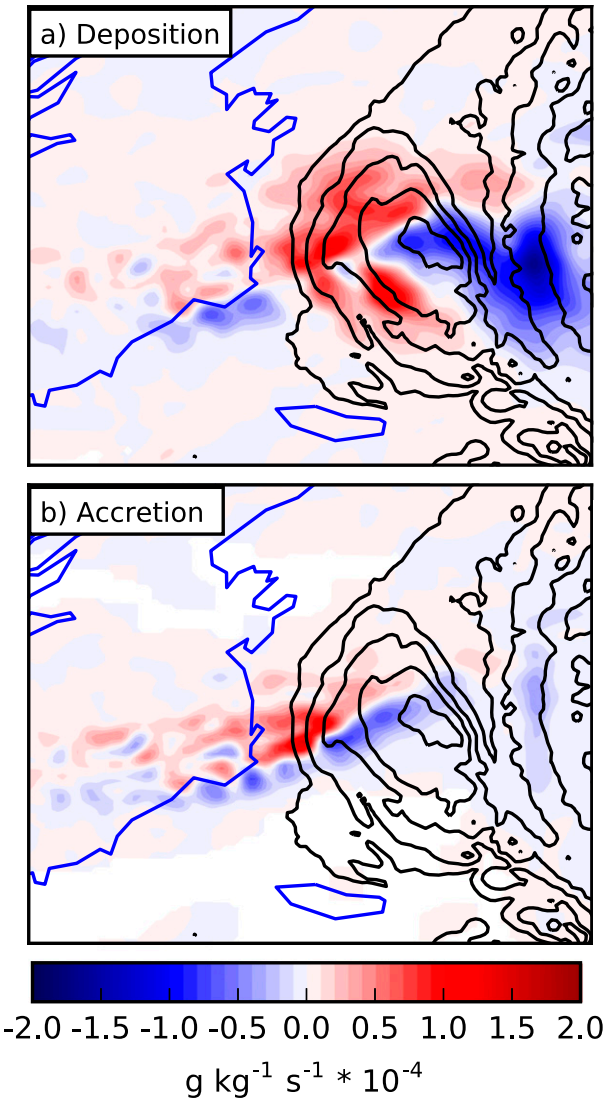

FIG. 14. Difference between Control and NoTug time-mean (0300–2200 UTC 11 Dec) 1000-m hydrometeor mass tendencies from (a) deposition (g kg^{-1} s^{-1}, color filled following scale at bottom) and (b) accretion [as in (a)]. Control topography (m MSL) contoured every 100 m. Blue lines indicate shorelines. Smoothed using a seven-point spectral cowbell filter (Barnes et al. 1996).

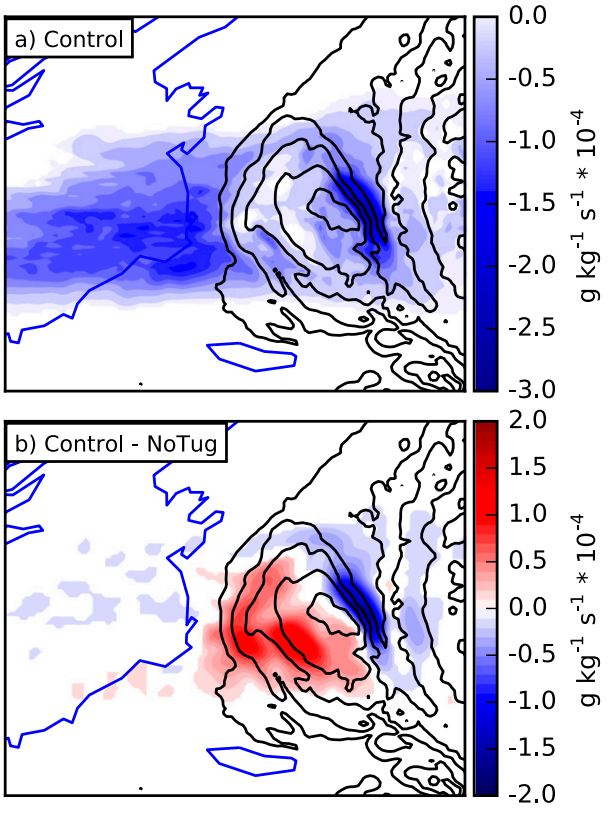

FIG. 15. (a) Control time-mean (0300–2200 UTC 11 Dec) lowest-half-η-level hydrometeor mass tendency due to sublimation (g kg^{-1} s^{-1}, color filled following scale at right). (b) Difference between Control and NoTug hydrometeor mass tendency (g kg^{-1} s^{-1}, color filled following scale at right). Smoothed using a seven-point spectral cowbell filter (Barnes et al. 1996). Control topography (m MSL) contoured every 100 m. Blue lines indicate shorelines.

base (Figs. 13a and 15a). This reduction in sublimational losses from the coastal lowlands to the upper reaches of Tug Hill contributes to a larger orographic ratio, as hypothesized by Minder et al. (2015). In contrast, sublimational losses in NoTug occur throughout the inland region due to a lack of elevated terrain (Fig. 13b). One area where sublimation is enhanced in Control, however, is over the lee slopes of Tug Hill because of terrain-induced subsidence (Figs. 13a and 15a,b).

In summary, the differences between Control and NoTug point toward an orographic contribution to the enhancement of the banded precipitation maximum over Tug Hill. The broad, boomerang-shaped region of ascent over Tug Hill's convex windward slopes increased low-level relative humidity and depositional growth rates, leading to increased precipitation and reduced sublimation losses, the latter minimized over the highest elevations of Tug Hill, which extended above cloud base. Stronger ascent along LBF2 further increased accretional and depositional growth rates. Together, these processes broadened and strengthened the precipitation maximum over Tug Hill.

7. Conclusions

Using WRF simulations, this study has examined the mechanisms responsible for the lake-effect precipitation maximum observed over Tug Hill during IOP2b of the Ontario Winter Lake-effect Systems (OWLeS) field campaign. Our analysis shows that both nonorographic

and orographic mechanisms contribute to the maximum, including the mesoscale forcing produced along a quasi-stationary land-breeze front (LBF2), precipitation enhancement processes associated with a boomerang-shaped region of windward orographic ascent, and reduced sublimation over Tug Hill.

LBF2, a product of Lake Ontario's distinctive shoreline geometry and differential surface heating and roughness effects (Steenburgh and Campbell 2017), developed along the southeast shore of Lake Ontario, extended inland across Tug Hill, and cut obliquely across the lake-effect system. It separated warmer, lake-modified air, which was also preconditioned upstream over Lake Huron, from cooler, continental air that passed through the land bridge between Lakes Erie and Ontario and the lowlands south of Lake Ontario, avoiding lake modification. Observed data from meteorological stations and upper-air soundings confirm the existence of LBF2 over Tug Hill. Mesoscale ascent along LBF2 served as a locus for increased hydrometeor growth, which strengthened and broadened the lake-effect system over Tug Hill. Although weaker, such strengthening and broadening were also produced in a simulation in which Tug Hill was removed, suggesting that LBF2 is an important contributor to the Tug Hill precipitation maximum even in the absence of orographic lift. The influence of LBF2, combined with strong subsidence over the central and southern lee slopes of Tug Hill, also contributed to a shift in the orientation of the banded lake-effect precipitation maximum as it extended inland across Tug Hill and into the western Adirondacks.

A boomerang-shaped region of ascent over the convex windward slopes of Tug Hill further enhanced precipitation by increasing depositional growth over Tug Hill and accretional growth along LBF2. Sublimation, which reduced hydrometeor mass over Lake Ontario and the upstream lowlands, was weaker over the windward slopes of Tug Hill, where orographic ascent increased relative humidity and enhanced precipitation, and reached a minimum over the high terrain of Tug Hill, which extended above the cloud base. Together, these orographic effects further intensified and broadened the precipitation maximum over Tug Hill.

To our knowledge, the contribution of LBF2 to precipitation enhancement over Tug Hill has not been recognized previously. Previous studies over the Great Lakes highlight the role of land-breeze convergence in the initiation and organization of lake-effect convection (e.g., Passarelli and Braham 1981; Ballentine 1982; Hjelmfelt and Braham 1983; Peace and Sykes 1966), but do not describe the complex configuration of land-breeze fronts produced by the unique shoreline geometry of Lake Ontario during IOP2b, which enabled LBF2 to cut across and enhance precipitation produced by the lake-effect system. The intensification of land-falling sea-effect snowbands as they traverse land-breeze fronts off the west coast of Japan, as mentioned by Ishihara et al. 1989, is somewhat analogous, but to our knowledge the Japanese literature has not investigated this type of evolution, focusing instead on the generation of incipient snowbands by the convergence of warm, sea-modified westerly flow with colder land-breezes along the western Japanese coast (e.g., Ishihara et al. 1989; Tsuboki et al. 1989; Yoshihara et al. 2004; Eito et al. 2005). Perhaps most similar to the land-breeze front documented here is the offshore reintensification and shift in orientation of lake-effect bands over the Baltic Sea by land-breeze fronts generated along Sweden's eastern shoreline (Andersson and Gustafsson 1994). In contrast, LBF2 primarily impacted the IOP2b lake-effect system inland, sustaining and broadening precipitation generation even after the lake-effect system was no longer maintained by the warm surface of the lake.

The numerical simulations presented here provide some context for the observationally based findings provided by Minder et al. (2015), Campbell et al. (2016), and Welsh et al. (2016). These studies highlight a convective-to-stratiform transition from Lake Ontario to Tug Hill, which is consistent with both the transition from the warmer lake to the cooler land surface, as well as ascent along LBF2. Welsh et al. (2016) explain the latter mechanism using a conceptual model (their Fig. 1) showing stratiform lift over a shallow dome of cold air east of Lake Ontario, but were not able to conclude what formed the cold dome. We show here that it is the cooler air mass behind the southwest–northeast-oriented LBF2, which extends downstream and inland from the southeast shoreline, rather than a simpler two-dimensional contrast formed by differential heating and cooling across the leeward shoreline. In addition to this transition, the orographically forced low-level uplift and associated increase in deposition around the convex slopes of Tug Hill is consistent with the increase in echo coverage and the larger orographic ratio observed during nonbanded lake-effect periods, as well as the broadening of LLAP bands over Tug Hill (Campbell et al. 2016). Moreover, we confirm Minder et al. (2015)'s hypothesis that the orographic suppression of sublimation contributes to precipitation enhancement over Tug Hill. Sublimation has also been identified as a driver of orographic enhancement in simulations of sea-effect snowbands in Japan (Murakami et al. 1994; Saito et al. 1996).

Tug Hill features a pronounced climatological lake-effect precipitation maximum and a high frequency of

lake-effect events. Given that most lake-effect events over Tug Hill feature broadly similar large-scale conditions, it is likely that land-breeze fronts similar to LBF2 contribute to other events over Tug Hill, while the orographic effects identified here may contribute to a broader spectrum of events with and without land-breeze fronts. Future work should extend this analysis to other events and utilize idealized simulations to better understand the interplay between land-breeze and orographic forcings during lake-effect events over Lake Ontario and other bodies of water.

Acknowledgments. We thank Jim and Cindy Cheney, John and Cheryl Cheney, and Gerhardt and Diane Brosch for their indispensable assistance during OWLeS, as well as the many individuals whose participation made the OWLeS field project a success. NCAR/EOL maintained the OWLeS data repository. We gratefully acknowledge the provision of datasets, software, and/or computer time and services by NCEI, NCEP, NCAR, MesoWest, and the University of Utah Center for High Performance Computing. Comments from Peter Veals, Tyler West, and three anonymous reviewers improved the manuscript. John McMillen helped with edits to the WRF code. This material is based upon work supported by the National Science Foundation Grant AGS-1262090. Any opinions, findings, conclusions or recommendations expressed are those of the authors and do not necessarily reflect the views of the National Science Foundation.

REFERENCES

Alcott, T. I., and W. J. Steenburgh, 2013: Orographic influences on a Great Salt Lake–effect snowstorm. *Mon. Wea. Rev.*, **141**, 2432–2450, doi:10.1175/MWR-D-12-00328.1.

Andersson, T., and S. Nilsson, 1990: Topographically induced convective snowbands over the Baltic Sea and their precipitation distribution. *Wea. Forecasting*, **5**, 299–312, doi:10.1175/1520-0434(1990)005<0299:TICSOT>2.0.CO;2.

——, and N. Gustafsson, 1994: Coast of departure and coast of arrival: Two important concepts for the formation and structure of convective snowbands over seas and lakes. *Mon. Wea. Rev.*, **122**, 1036–1049, doi:10.1175/1520-0493(1994)122<1036:CODACO>2.0.CO;2.

Arnott, J., 2010: Examining a southward bias in lake-effect snow band forecasts in the Northeast Regional Ensemble. *Natl. Wea. Dig.*, **34**, 68–87.

Ballentine, R. J., 1982: Numerical simulation of land-breeze-induced snowbands along the western shore of Lake Michigan. *Mon. Wea. Rev.*, **110**, 1544–1553, doi:10.1175/1520-0493(1982)110<1544:NSOLBI>2.0.CO;2.

——, and D. Zaff, 2007: Improving the understanding and prediction of lake-effect snowstorms in the eastern Great Lakes region. Final Rep. to the COMET Outreach Program, UCAR Award S06-58395, 41 pp. [Available online at http://www.comet.ucar.edu/outreach/details.php?id=2111.]

Barnes, S. L., F. Caracena, and A. Marroquin, 1996: Extracting synoptic-scale diagnostic information from mesoscale models: The Eta model, gravity waves, and quasigeostrophic diagnostics. *Bull. Amer. Meteor. Soc.*, **77**, 519–528, doi:10.1175/1520-0477(1996)077<0519:ESSDIF>2.0.CO;2.

Bergeron, T., 1965: On the low-level redistribution of atmospheric water caused by orography. *Proc. Int. Conf. on Cloud Physics*, Toronto, ON, Canada, Amer. Meteor. Soc., 96–100.

Bergmaier, P. T., B. Geerts, L. S. Campbell, and W. J. Steenburgh, 2017: The OWLeS IOP2b lake-effect snowstorm: Dynamics of the secondary circulation. *Mon. Wea. Rev.*, **145**, 2437–2459, doi:10.1175/MWR-D-16-0462.1.

Browning, K. H., F. F. Hill, and C. W. Pardoe, 1974: Structure and mechanism of precipitation and the effect of orography in wintertime warm sector. *Quart. J. Roy. Meteor. Soc.*, **100**, 309–330, doi:10.1002/qj.49710042505.

Campbell, L. S., P. G. Veals, T. W. Letcher, and J. R. Minder, 2016: Lake-effect mode and precipitation enhancement over the Tug Hill Plateau during OWLeS IOP2b. *Mon. Wea. Rev.*, **144**, 1729–1748, doi:10.1175/MWR-D-15-0412.1.

Carpenter, D. M., 1993: The lake effect of the Great Salt Lake: Overview and forecast problems. *Wea. Forecasting*, **8**, 181–193, doi:10.1175/1520-0434(1993)008<0181:TLEOTG>2.0.CO;2.

Chen, F., and J. Dudhia, 2001: Coupling an advanced land surface–hydrology model with the Penn State–NCAR MM5 modeling system. Part II: Preliminary model validation. *Mon. Wea. Rev.*, **129**, 587–604, doi:10.1175/1520-0493(2001)129<0587:CAALSH>2.0.CO;2.

Colle, B. A., Y. Lin, S. Medina, and B. F. Smull, 2008: Orographic modification of convection and flow kinematics by the Oregon Coast Range and Cascades during IMPROVE-2. *Mon. Wea. Rev.*, **136**, 3894–3916, doi:10.1175/2008MWR2369.1.

——, R. B. Smith, and D. A. Wesley, 2013: Theory, observations, and predictions of orographic precipitation. *Mountain Weather Research and Forecasting: Recent Progress and Current Challenges*, F. K. Chow, S. F. J. De Wekker, and B. J. Snyder, Eds., Springer Atmospheric Sciences, Springer, 291–344.

Conrick, R., H. D. Reeves, and S. Zhong, 2015: The dependence of QPF on the choice of boundary and surface layer parameterization for a lake-effect snowstorm. *J. Appl. Meteor. Climatol.*, **54**, 1177–1190, doi:10.1175/JAMC-D-14-0291.1.

Crum, T. D., R. L. Alberty, and D. W. Burgess, 1993: Recording, archiving, and using WSR-88D data. *Bull. Amer. Meteor. Soc.*, **74**, 645–653, doi:10.1175/1520-0477(1993)074<0645:RAAUWD>2.0.CO;2.

Dudhia, J., 1989: Numerical study of convection observed during the Winter Monsoon Experiment using a mesoscale two-dimensional model. *J. Atmos. Sci.*, **46**, 3077–3107, doi:10.1175/1520-0469(1989)046<3077:NSOCOD>2.0.CO;2.

Eito, H., T. Kato, M. Yoshizaki, and A. Adachi, 2005: Numerical simulation of the quasi- stationary snowband observed over the southern coastal area of the Sea of Japan on 16 January 2001. *J. Meteor. Soc. Japan*, **83**, 551–576, doi:10.2151/jmsj.83.551.

Hill, J. D., 1971: Snow squalls in the lee of Lakes Erie and Ontario. NOAA Tech. Memo. NWS ER-43, 20 pp.

Hjelmfelt, M. R., 1992: Orographic effects in simulated lake-effect snowstorms over Lake Michigan. *Mon. Wea. Rev.*, **120**, 373–377, doi:10.1175/1520-0493(1992)120<0373:OEISLE>2.0.CO;2.

——, and R. R. Braham Jr., 1983: Numerical simulation of the airflow over Lake Michigan for a major lake-effect snow event. *Mon. Wea. Rev.*, **111**, 205–219, doi:10.1175/1520-0493(1983)111<0205:NSOTAO>2.0.CO;2.

Hong, S.-Y., Y. Noh, and J. Dudhia, 2006: A new vertical diffusion package with an explicit treatment of entrainment processes. *Mon. Wea. Rev.*, **134**, 2318–2341, doi:10.1175/MWR3199.1.

Houze, R., 2012: Orographic effects on precipitating clouds. *Rev. Geophys.*, **50**, 1–47, doi:10.1029/2011RG000365.

Iacono, M. J., J. S. Delamere, E. J. Mlawer, M. W. Shephard, S. A. Clough, and W. D. Collins, 2008: Radiative forcing by long-lived greenhouse gases: Calculations with the AER radiative transfer models. *J. Geophys. Res.*, **113**, D13103, doi:10.1029/2008JD009944.

Ishihara, M., H. Sakakibara, and Z. Yanagisawa, 1989: Doppler radar analysis of the structure of mesoscale snow bands developed between the winter monsoon and the land breeze. *J. Meteor. Soc. Japan*, **67**, 503–520.

Jiménez, P. A., J. Dudhia, J. F. González-Rouco, J. Navarro, J. P. Montávez, and E. García-Bustamante, 2012: A revised scheme for the WRF surface layer formulation. *Mon. Wea. Rev.*, **140**, 898–918, doi:10.1175/MWR-D-11-00056.1.

Kain, J. S., 2004: The Kain–Fritsch convective parameterization: An update. *J. Appl. Meteor.*, **43**, 170–181, doi:10.1175/1520-0450(2004)043<0170:TKCPAU>2.0.CO;2.

Kindap, T., 2010: A severe sea-effect snow episode over the city of Istanbul. *Nat. Hazards*, **54**, 707–723, doi:10.1007/s11069-009-9496-7.

Kirshbaum, D. J., and A. L. M. Grant, 2012: Invigoration of cumulus cloud fields by mesoscale ascent. *Quart. J. Roy. Meteor. Soc.*, **138**, 2136–2150, doi:10.1002/qj.1954.

Kristovich, D. A. R., and Coauthors, 2017: The Ontario Winter Lake-Effect Systems Field Campaign: Scientific and educational adventures to further our knowledge and prediction of lake-effect storms. *Bull. Amer. Meteor. Soc.*, **98**, 315–332, doi:10.1175/BAMS-D-15-00034.1.

Laird, N., J. Desrochers, and M. Payer, 2009: Climatology of lake-effect precipitation events over Lake Champlain. *J. Appl. Meteor. Climatol.*, **48**, 232–250, doi:10.1175/2008JAMC1923.1.

——, R. Sobash, and N. Hodas, 2010: Climatological conditions of lake-effect precipitation events associated with the New York State Finger Lakes. *J. Appl. Meteor. Climatol.*, **49**, 1052–1062, doi:10.1175/2010JAMC2312.1.

McMillen, J. D., and W. J. Steenburgh, 2015a: Impact of microphysics parameterizations on simulations of the 27 October 2010 Great Salt Lake-effect snowstorm. *Wea. Forecasting*, **30**, 136–152, doi:10.1175/WAF-D-14-00060.1.

——, and ——, 2015b: Capabilities and limitations of convection-permitting WRF simulations of lake-effect systems over the Great Salt Lake. *Wea. Forecasting*, **30**, 1711–1731, doi:10.1175/WAF-D-15-0017.1.

Minder, J. R., R. B. Smith, and A. D. Nugent, 2013: The dynamics of ascent-forced orographic convection in the tropics: Results from Dominica. *J. Atmos. Sci.*, **70**, 4067–4088, doi:10.1175/JAS-D-13-016.1.

——, T. W. Letcher, L. S. Campbell, P. V. Veals, and W. J. Steenburgh, 2015: The evolution of lake-effect convection during landfall and orographic uplift as observed by profiling radars. *Mon. Wea. Rev.*, **143**, 4422–4442, doi:10.1175/MWR-D-15-0117.1.

Murakami, M., T. L. Clark, and W. D. Hall, 1994: Numerical simulations of convective snow clouds over the Sea of Japan; Two-dimensional simulations of mixed layer development and convective snow cloud formation. *J. Meteor. Soc. Japan*, **72**, 43–62.

Nakai, S., and T. Endoh, 1995: Observation of snowfall and airflow over a low mountain barrier. *J. Meteor. Soc. Japan*, **73**, 183–199.

Norton, D. C., and S. J. Bolsenga, 1993: Spatiotemporal trends in lake effect and continental snowfall in the Laurentian Great Lakes, 1951–1980. *J. Climate*, **6**, 1943–1956, doi:10.1175/1520-0442(1993)006<1943:STILEA>2.0.CO;2.

Passarelli, R. E. J., and R. R. J. Braham, 1981: The role of the winter land breeze in the formation of Great Lake snow storms. *Bull. Amer. Meteor. Soc.*, **62**, 482–491, doi:10.1175/1520-0477(1981)062<0482:TROTWL>2.0.CO;2.

Peace, R. L., and R. B. Sykes, 1966: Mesoscale study of a lake-effect snowstorm. *Mon. Wea. Rev.*, **94**, 495–507, doi:10.1175/1520-0493(1966)094<0495:MSOALE>2.3.CO;2.

Reeves, H. D., and D. T. Dawson, 2013: The dependence of QPF on the choice of microphysical parameterization for lake-effect snowstorms. *J. Appl. Meteor. Climatol.*, **52**, 363–377, doi:10.1175/JAMC-D-12-019.1.

Roe, G. H., 2005: Orographic precipitation. *Annu. Rev. Earth Planet. Sci.*, **33**, 645–671, doi:10.1146/annurev.earth.33.092203.122541.

Saito, K., M. Murakami, T. Matsuo, and H. Mizuno, 1996: Sensitivity experiments on the orographic snowfall over the mountainous region of northern Japan. *J. Meteor. Soc. Japan*, **74**, 797–813.

Schmidlin, T. W., 1993: Impacts of severe winter weather during December 1989 in the Lake Erie snowbelt. *J. Climate*, **6**, 759–767, doi:10.1175/1520-0442(1993)006<0759:IOSWWD>2.0.CO;2.

Shi, J. J., and Coauthors, 2010: WRF simulations of the 20–22 January 2007 snow events over eastern Canada: Comparison with in situ and satellite observations. *J. Appl. Meteor. Climatol.*, **49**, 2246–2266, doi:10.1175/2010JAMC2282.1.

Skamarock, W. C., and J. B. Klemp, 2008: A time-split non-hydrostatic atmospheric model for weather research and forecasting applications. *J. Comput. Phys.*, **227**, 3465–3485, doi:10.1016/j.jcp.2007.01.037.

Smith, R. B., 2006: Progress on the theory of orographic precipitation. *Special Paper 398: Tectonics, Climate, and Landscape Evolution*, Geological Society of America, Boulder, CO, 1–16.

——, Q. Jiang, M. G. Fearon, P. Tabary, M. Dorninger, J. D. Doyle, and R. Benoit, 2003: Orographic precipitation and air mass transformation: An Alpine example. *Quart. J. Roy. Meteor. Soc.*, **129**, 433–454, doi:10.1256/qj.01.212.

——, P. Schafer, D. J. Kirshbaum, and E. Regina, 2009: Orographic precipitation in the tropics: Experiments in Dominica. *J. Atmos. Sci.*, **66**, 1698–1716, doi:10.1175/2008JAS2920.1.

Steenburgh, W. J., and D. J. Onton, 2001: Multiscale analysis of the 7 December 1998 Great Salt Lake–effect snowstorm. *Mon. Wea. Rev.*, **129**, 1296–1317, doi:10.1175/1520-0493(2001)129<1296:MAOTDG>2.0.CO;2.

——, and L. S. Campbell, 2017: The OWLeS IOP2b lake-effect snowstorm: Shoreline geometry and the mesoscale forcing of precipitation. *Mon. Wea. Rev.*, **145**, 2421–2436, doi:10.1175/MWR-D-16-0460.1.

——, S. F. Halvorson, and D. J. Onton, 2000: Climatology of lake-effect snowstorms of the Great Salt Lake. *Mon. Wea. Rev.*, **128**, 709–727, doi:10.1175/1520-0493(2000)128<0709:COLESO>2.0.CO;2.

Stoelinga, M. T., R. E. Stewart, G. Thompson, and J. Theriault, 2013: Microphysical processes within winter orographic cloud and precipitation systems. *Mountain Weather Research and Forecasting: Recent Progress and Current Challenges*, F. K. Chow, S. F. J. De Wekker, and B. J. Snyder, Eds., Springer Atmospheric Sciences, Springer, 345–408.

Theeuwes, N. E., G. J. Steeneveld, F. Krikken, and A. A. M. Holtslag, 2010: Mesoscale modeling of lake-effect snow over

Lake Erie, sensitivity to convection, microphysics and the water temperature. *Adv. Sci. Res.*, **4**, 15–22, doi:10.5194/asr-4-15-2010.

Thompson, G., P. R. Field, R. M. Rasmussen, and W. D. Hall, 2008: Explicit forecasts of winter precipitation using an improved bulk microphysics scheme. Part II: Implementation of a new snow parameterization. *Mon. Wea. Rev.*, **136**, 5095–5114, doi:10.1175/2008MWR2387.1.

Tsuboki, K., Y. Fujiyoshi, and G. Wakahama, 1989: Doppler radar observation of convergence band cloud formed on the west coast of Hokkaido Island. II: Cold frontal type. *J. Meteor. Soc. Japan*, **67**, 985–999.

Veals, P. G., and W. J. Steenburgh, 2015: Climatological characteristics and orographic enhancement of lake-effect precipitation east of Lake Ontario and over the Tug Hill Plateau. *Mon. Wea. Rev.*, **143**, 3591–3609, doi:10.1175/MWR-D-15-0009.1.

Watson, C. D., and T. P. Lane, 2012: Sensitivities of orographic precipitation to terrain geometry and upstream conditions in idealized simulations. *J. Atmos. Sci.*, **69**, 1208–1231, doi:10.1175/JAS-D-11-0198.1.

Welsh, D., B. Geerts, X. Jing, P. T. Bergmaier, J. R. Minder, W. J. Steenburgh, and L. S. Campbell, 2016: Understanding heavy lake-effect snowfall: The vertical structure of radar reflectivity in a deep snowband over and downwind of Lake Ontario. *Mon. Wea. Rev.*, **144**, 4221–4244, doi:10.1175/MWR-D-16-0057.1.

Wüest, M., C. Frei, A. Altenhoff, M. Hagen, M. Litschi, and C. Schar, 2010: A gridded hourly precipitation dataset for Switzerland using rain-gauge analysis and radar-based disaggregation. *Int. J. Climatol.*, **30**, 1764–1775.

Yeager, K. N., W. J. Steenburgh, and T. I. Alcott, 2013: Contributions of lake-effect periods to the cool-season hydroclimate of the Great Salt Lake basin. *J. Appl. Meteor. Climatol.*, **52**, 341–362, doi:10.1175/JAMC-D-12-077.1.

Yoshihara, H., M. Kawashima, K. I. Arai, J. Inoue, and Y. Fujiyoshi, 2004: Doppler radar study on the successive development of snowbands at a convergence line near the coastal region of Hokuriku district. *J. Meteor. Soc. Japan*, **82**, 1057–1079.

Yuter, S., and R. A. Houze, 1995: Three-dimensional kinematic and microphysical evolution of Florida cumulonimbus. Part II: Frequency distributions of vertical velocity, reflectivity, and differential reflectivity. *Mon. Wea. Rev.*, **123**, 1941–1963, doi:10.1175/1520-0493(1995)123<1941:TDKAME>2.0.CO;2.